

Screw dislocation in zirconium: an *ab initio* study

Emmanuel Clouet*

CEA, DEN, Service de Recherches de Métallurgie Physique, 91191 Gif-sur-Yvette, France

(Dated: November 7, 2018)

Plasticity in zirconium is controlled by $1/3\langle 1\bar{2}10 \rangle$ screw dislocations gliding in the prism planes of the hexagonal close-packed structure. This prismatic and not basal glide is observed for a given set of transition metals like zirconium and is known to be related to the number of valence electrons in the d band. We use *ab initio* calculations based on the density functional theory to study the core structure of screw dislocations in zirconium. Dislocations are found to dissociate in the prism plane in two partial dislocations, each with a pure screw character. *Ab initio* calculations also show that the dissociation in the basal plane is unstable. We calculate then the Peierls barrier for a screw dislocation gliding in the prism plane and obtain a small barrier. The Peierls stress deduced from this barrier is lower than 21 MPa, which is in agreement with experimental data. The ability of an empirical potential relying on the embedded atom method (EAM) to model dislocations in zirconium is also tested against these *ab initio* calculations.

PACS numbers: 61.72.Lk, 61.72.Bb

I. INTRODUCTION

Plasticity in α -zirconium is controlled by dislocations with a $1/3\langle 1\bar{2}10 \rangle$ Burgers vector gliding in the prism planes of the hexagonal compact (hcp) lattice.^{1–4} The relative ease of prismatic glide compared to basal glide has been shown to be linked to the ratio of the corresponding stacking fault energies, which in turn is controlled by the electronic structure.⁵ In particular, Legrand⁵ used a tight binding model to show that prismatic slip in transition metals of the IV B column (Zr, Ti, Hf) originates from the electronic filling of the valence d band. As a consequence, it appears necessary to take into account the anisotropy of the d orbital, and hence the angular dependence of the atomic bonding, to model dislocations in these transition metals⁶. One cannot therefore rely on central forces empirical potential and needs to take account of the electronic structure. Tight binding models^{7,8} or *ab initio* calculations^{9–13} show indeed that a $1/3\langle 1\bar{2}10 \rangle$ screw dislocation, either in Zr or in Ti, spreads in prism planes, in agreement with the prismatic glide observed experimentally. But none of these atomistic simulations calculate the Peierls stress of a screw dislocation. According to some authors,^{7,14} its core structure is not completely planar, which may be the cause of a high Peierls stress.

It is true, experimentally, that screw dislocations glide with difficulty compared to other dislocation characters in zirconium or titanium alloys: characteristic microstructures, with long and straight dislocations aligned along their screw orientation, are observed at low temperature,^{3,9,15–18} and the flow stress is strongly temperature dependent,^{2,3,16,19–23} in agreement with the assumption of a high Peierls barrier which must be overcome by the nucleation of double kinks. But experiments also show that the yield stress in zirconium or in titanium strongly decreases with a decreasing amount of interstitial impurities like oxygen.^{2,3,16,19,22,23} It is therefore probable that the high Peierls stress of screw dis-

locations has an extrinsic cause. In pure zirconium or pure titanium, this Peierls stress may not be as high and screw dislocations are probably gliding as easily as other orientations.

Recently, Mendelev and Ackland²⁴ developed an empirical potential for Zr in the Embedded Atom Method (EAM) formalism. Using this potential, Khater and Bacon²⁵ showed that it leads to a screw dislocation that spontaneously spreads in the prism plane, the configuration dissociated in the basal plane being metastable. They also showed that the Peierls stress of a screw dislocation gliding in the prism plane is not so different from the Peierls stress of an edge dislocation and that this stress is small (22 MPa for the screw and 16 MPa for the edge). These results therefore support experimental findings stating that screw dislocations are gliding in prism planes with a low Peierls stress in pure zirconium. But these simulations rely on a central forces potential, which is not well suited to describe dislocations in a hcp transition metal like Zr, as described above. More reliable atomistic simulations, incorporating a description of the electronic structure, are therefore needed to confirm this easy glide of screw dislocations in pure zirconium.

This article aims to use *ab initio* calculations so as to fully characterize the core structure of a $1/3\langle 1\bar{2}10 \rangle$ screw dislocation in zirconium and estimate its Peierls stress. We also examine generalized stacking faults as dislocation core structures are closely related to them. Two different *ab initio* methods, SIESTA²⁶ and PWSCF²⁷, have been used. SIESTA offers the advantage of efficiency, allowing simulating more atoms than with a standard *ab initio* code, whereas PWSCF offers the advantage of robustness. All calculations are also performed with Mendelev and Ackland EAM potential,²⁴ so as to identify its ability to model dislocations in zirconium. In addition, this empirical potential is used to study the convergence of our results with the size of the simulation cell.

II. ATOMIC INTERACTION MODELING

Atomistic simulations have been performed both with an empirical interatomic potential and with *ab initio* calculations. The empirical potential that we used is the EAM potential developed by Mendelev and Ackland.²⁴ This potential is labeled #3 in Ref. 24. It is supposed to be well suited to model dislocations, as *ab initio* values²⁸ of the stacking fault energies in the basal and prism planes have been included in the fitting procedure. Using this potential, Khater and Bacon²⁵ showed that a $1/3 \langle 1\bar{2}10 \rangle$ screw dislocation spontaneously dissociates in the prism plane and that a metastable configuration dissociated in the basal plane also exists.

The *ab initio* calculations are relying on the Density Functional Theory (DFT) in the Generalized Gradient Approximation (GGA) with the functional proposed by Perdew, Burke, and Ernzerhof (PBE) and the pseudopotential approximation. Two different *ab initio* codes are used, SIESTA²⁶ and PWSCF.²⁷

In the SIESTA code,²⁶ valence electrons are described by a localized basis set corresponding to a linear combination of pseudoatomic orbitals with 13 functions per atom. We used a norm conserving pseudopotential of Troulliers-Martins type with 4p electrons included as semicore. Electronic density of state is broadened with the Methfessel-Paxton function with a broadening of 0.3 eV and the integration is performed on a regular grid of $14 \times 14 \times 8$ k-points for the primitive hcp unit cell and an equivalent density of k-points for the supercells used for the defect calculations. The charge density is represented on a real space grid with a spacing of 0.08 Å (Mesh cutoff: 450 Ry) that is reduced to 0.06 Å (800 Ry) for dislocation calculations. This approach, *i.e.* the basis and the pseudopotential, has already been used to study vacancy diffusion in zirconium²⁹ and comparison with plane waves DFT calculations has led to a reasonable agreement.

In the PWSCF code,²⁷ valence electrons are described with plane waves using a cutoff energy of 28 Ry. The pseudopotential is ultrasoft of Vanderbilt type with 4s and 4p electrons included as semicore.³⁰ The same k-point grid and the same electronic broadening are used as with SIESTA code.

To validate these different atomic interaction models, it is worth comparing their results to available experimental data for some bulk properties of Zr. All models lead to an equilibrium lattice parameter and a c/a ratio in good agreement with experimental data (Tab. I). In particular, a ratio lower than the ideal $\sqrt{8/3} \sim 1.633$ value is obtained in all cases.

We also compared the theoretical elastic constants with experimental data (Tab. I): a good agreement is also obtained. The computed elastic constants are the relaxed ones:³⁵ as the hcp lattice contains two atoms in its primitive unit cell, some internal degrees of freedom may exist when applying a homogeneous strain. One needs to allow for atomic relaxations when computing C_{11} , C_{12} or C_{66} constants.³¹ It is also possible to calculate inner elastic

TABLE I. Bulk properties of hcp Zr calculated with different atomic interaction models and compared to experimental data: lattice parameter a , c/a ratio of the hexagonal lattice, relaxed elastic constants C_{ij} , inner elastic constants³¹ e_{ij} and d_{ij} , phonon frequencies ω_1 and ω_3 of the optical branches at the Γ point (Eq. 1), inner elasticity contribution to elastic constant δC_{12} (Eq. 2).

	Expt.	EAM	SIESTA	PWSCF
a (Å)	3.232 ³²	3.234	3.237	3.230
c/a	1.603 ³²	1.598	1.613	1.601
C_{11} (GPa)	155.4 ^a	142.	140.	140.
C_{33} (GPa)	172.5 ^a	168.	168.	168.
C_{12} (GPa)	67.2 ^a	75.	86.	70.
C_{13} (GPa)	64.6 ^a	76.	68.	65.
C_{44} (GPa)	36.3 ^a	44.	24.	26.
C_{66} (GPa)	44.1 ^a	33.5	27.	35.
e_{11} (meV Å ⁻⁵)		27.0	17.0	18.6
e_{33} (meV Å ⁻⁵)		118.	122.	101.
d_{21} (meV Å ⁻⁴)		30.0	38.9	36.6
ω_1 (THz)	2.66 ± 0.02^{33}	2.60	2.08	2.16
ω_3 (THz)	4.23 ± 0.15^{33}	5.43	5.57	5.03
δC_{12} (GPa)		5.33	14.3	11.5

^a Experimental elastic constants³⁴ have been measured at 4 K.

constants to characterize these internal degrees of freedom. These are also given in Tab. I using the notations introduced by Cousins.³¹ Two of these inner elastic constants, e_{11} and e_{33} , are related to the phonon frequencies of the optical branches at the Γ point³¹

$$\omega_i = 2\sqrt{\frac{\Omega e_{ii}}{m}}, \quad (1)$$

where $\Omega = a^2 c \sqrt{3}/4$ is the atomic volume and m the atomic mass. The last inner elastic constants d_{21} couples the internal degrees of freedom to the homogeneous strain. It leads to a contribution to the elastic constants³¹

$$\delta C_{12} = \frac{d_{21}^2}{e_{11}}. \quad (2)$$

If C_{ij}^0 are the unrelaxed elastic constants, *i.e.* the elastic constants calculated by imposing a homogeneous strain to the hcp lattice without letting atoms relax from their initial positions, the true elastic constants are given by³¹ $C_{11} = C_{11}^0 - \delta C_{12}$, $C_{12} = C_{12}^0 + \delta C_{12}$, and $C_{66} = C_{66}^0 - \delta C_{12}$, all other elastic constants being unchanged.

III. STACKING FAULT ENERGIES

Dislocation dissociation is controlled by the existence of a metastable stacking fault for the corresponding plane. According to the results obtained by Khater and Bacon²⁵ with Mendelev and Ackland EAM potential,²⁴

TABLE II. Stacking fault energies in the basal plane, γ_b , and in the prism plane, γ_p , calculated with different atomic interaction models, including VASP calculations of Domain *et al.*²⁸ and of Udagawa *et al.*³⁷ R is the ratio defined by Legrand,⁵ and d_b^{eq} and d_p^{eq} are the dissociation lengths of a screw dislocation respectively in the basal (Eq. 5) and in the prism plane (Eq. 6).

	EAM	SIESTA	PWSCF	VASP ²⁸	VASP ³⁷
γ_b (mJ m ⁻²)	198.	199.	213.	200.	227.
γ_p (mJ m ⁻²)	135. (274.) ^a	233.	211.	145.	197.
$R = C_{66}\gamma_b/C_{44}\gamma_p$	1.12	0.96	1.36	1.85	2.1
d_b^{eq} (Å)	4.0	2.0	2.7	3.4	3.2
d_p^{eq} (Å)	7.8	4.6	5.9	9.6	7.4

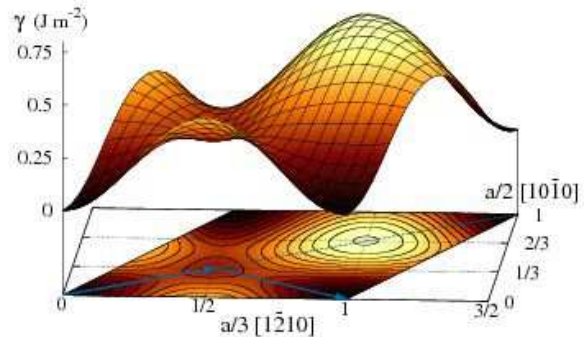
^a For the EAM calculation of the prismatic stacking fault energy, the value in parenthesis corresponds to the maximum in $a/6[1\bar{2}10]$, whereas the lower value corresponds to the true minimum in $a/6[1\bar{2}10] + 0.14c[0001]$.

a $1/3\langle 1\bar{2}10 \rangle$ screw dislocation can dissociate either in a basal or in a prism plane. To characterize these eventual dissociations, we compute generalized stacking fault energies^{14,36} – or γ -surfaces – for both the basal and the prism planes.

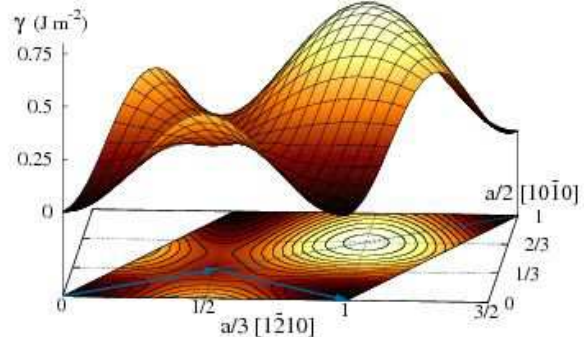
A. Methodology

γ -surfaces describe the energy variation when two parts of a crystal are rigidly shifted for different fault vectors lying in a given crystallographic plane. Atoms are allowed to relax in the direction perpendicular to the fault plane. We calculate these γ -surfaces for both the basal and prism planes using full periodic boundary conditions. To introduce only one fault in the simulation cell, the same shift as the one corresponding to the fault vector is applied to the periodicity vector perpendicular to the fault plane. No free surfaces is therefore introduced in the simulation cell, which allows a fast convergence of the fault energies with the number of stacked planes. A periodic stacking of at least 16 $\{0001\}$ planes is used for the basal fault and 12 $\{10\bar{1}0\}$ planes for the prismatic fault. This corresponds to a distance between fault planes $h_{0001} = 8c \sim 41$ Å and $h_{10\bar{1}0} = 6\sqrt{3}a \sim 34$ Å. Increasing the number of planes in the stacking modifies the energies by less than 1 mJ m⁻². Generalized stacking fault energies are calculated on a regular grid of 10×10 fault vectors and are then interpolated with Fourier series.

(a) Pwscf - basal plane



(b) Siesta - basal plane



(c) EAM - basal plane

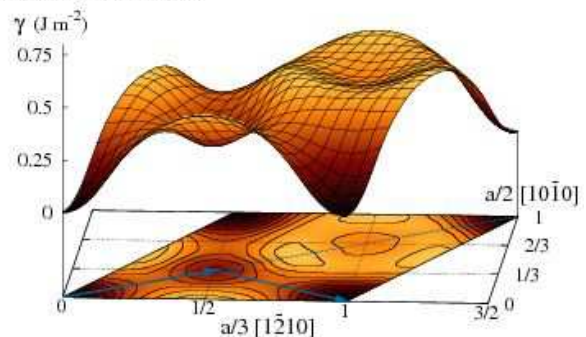


FIG. 1. Generalized stacking fault energy in the basal plane calculated with (a) PWSCF, (b) SIESTA and (c) EAM potential. The arrows indicate Burgers vectors of the partial dislocations corresponding to a dissociation in the basal plane. The dashed line is the $[1\bar{1}00]$ direction used in Fig. 2. Contour lines are drawn at the base every 50 mJ m⁻².

B. γ -surfaces

1. Basal plane

γ -surfaces corresponding to the basal plane are shown in Fig. 1 for the three interaction models we used. In all cases, a local minimum can be found at $1/3[1\bar{1}00]$ which corresponds to the intrinsic I_2 fault.³⁸ This minimum does not vary when full atomic relaxations are allowed

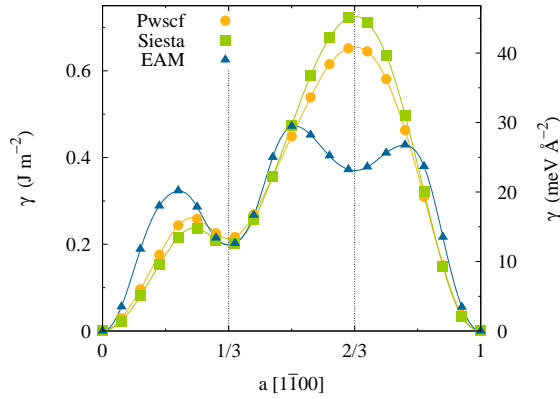


FIG. 2. Generalized stacking fault energy in the basal plane along the $[1\bar{1}00]$ direction (*cf.* Fig. 1) calculated with PWSCF, SIESTA and EAM potential.

instead of being constrained to the direction perpendicular to the fault plane. All methods give a close value for the fault energy γ_b in this minimum (Tab. II). A good agreement is also obtained with the values calculated by Domain *et al.*²⁸ and by Udagawa *et al.*³⁷ using VASP *ab initio* code. The depth of this local minimum is more pronounced with the empirical EAM potential [Fig. 1(c)] than in *ab initio* calculations [Fig. 1(a) and (b)]. This appears clearly in Fig. 2 where the fault energy predicted by the different interaction models are compared along the $[1\bar{1}00]$ direction. We will see latter that this has consequences on the stability of a screw dislocation dissociated in the basal plane.

The γ -surface calculated with the EAM empirical potential has another minimum located in $2/3[1\bar{1}00]$. This is an artifact of the potential: one expects instead a maximum as this fault vector transforms the original BABABA stacking of the basal planes in a BABBCB stacking. *Ab initio* calculations confirm that this fault vector gives a maximum. Finally, it is worth pointing that both *ab initio* techniques give a very similar γ -surface: the shapes are identical and the amplitudes do not differ by more than 10%.

2. Prism plane

γ -surfaces for the prism plane are shown in Fig. 3. Both *ab initio* methods lead to a similar γ -surface [Figs. 3(a) and (b)]. In particular, both PWSCF and SIESTA predicts the existence of a minimum at halfway of the Burgers vector, *i.e.* in $1/6[1\bar{2}10]$. Like for the basal fault, this minimum does not vary when full atomic relaxations are allowed. As can be seen on the projection of these γ -surface along the $[1\bar{2}10]$ direction (Fig. 4), this minimum is a little more pronounced with PWSCF than with SIESTA. The same minimum was also present in the VASP calculations of Domain *et al.*,²⁸ but they obtained a lower value γ_p of the fault energy in this point (Tab. II).

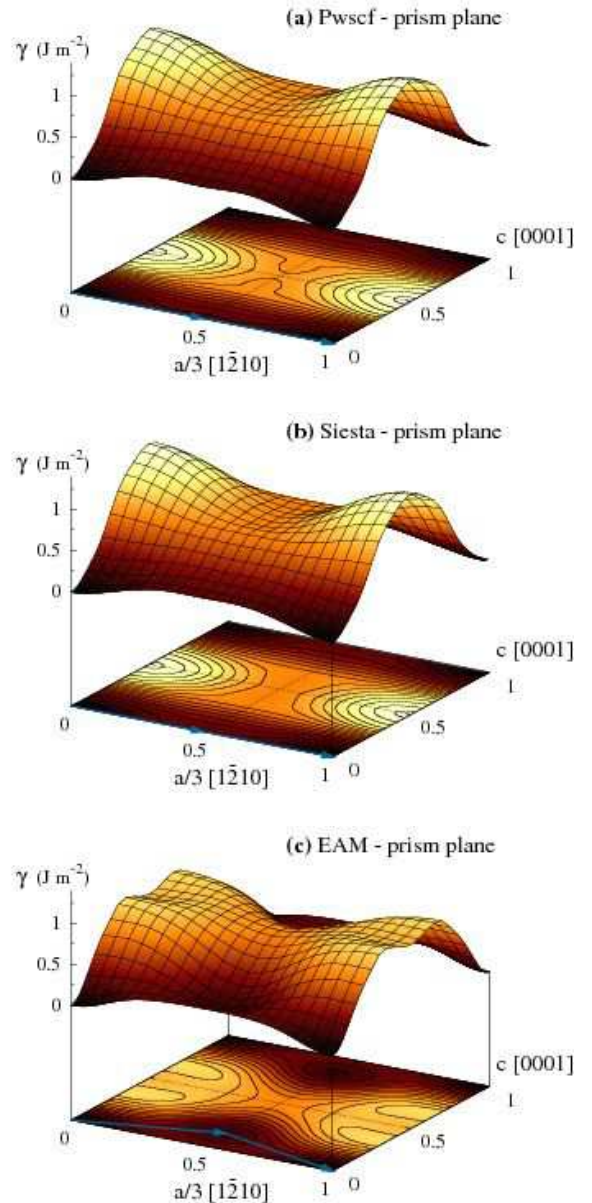


FIG. 3. Generalized stacking fault energy in the prism plane calculated with (a) PWSCF, (b) SIESTA and (c) EAM potential. The arrows indicate Burgers vectors of the partial dislocations corresponding to a dissociation in the prism plane. Contour lines are drawn at the base every 75 mJ m^{-2} .

On the other hand, Udagawa *et al.*³⁷ obtained a value close to our result using also VASP *ab initio* code with the PAW method and the PBE-GGA functional. They pointed out that the discrepancy arises from an insufficient number of stacked planes in the γ -surface calculation of Domain *et al.*. The energy of the metastable stacking fault energy in the prism plane appears therefore higher than the value 145 mJ m^{-2} initially suggested by Domain *et al.*:²⁸ both our PWSCF³⁹ and SIESTA calculations, as well as the Udagawa *et al.* result,³⁷ leads to

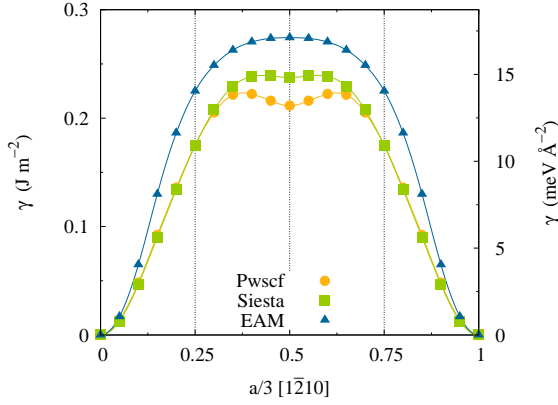


FIG. 4. Generalized stacking fault energy in the prism plane along the $[1\bar{2}10]$ direction calculated with PWSCF, SIESTA and EAM potential.

a value of about 200 mJ m^{-2} .

The γ -surface calculated with the EAM potential is quite different [Fig. 3(c)] as the point located in $1/6 [1\bar{2}10]$ is indeed a maximum and not a minimum like with *ab initio* calculations. A minimum is found for a point located in $a/6 [1\bar{2}10] + 0.14c [0001]$. One therefore expects that a $1/3[1\bar{2}10] \{10\bar{1}0\}$ dislocation dissociates into two partial dislocations with a Burgers vector component orthogonal to the one of the perfect dislocation. In particular, a screw dislocation should dissociate in two partial dislocations with a small edge character. Khater and Bacon²⁵ showed that the empirical potential of Ackland *et al.*⁴⁰ suffers from the same artefact. As noted by Bacon and Vitek,⁴¹ all central forces potentials stabilize indeed such a stacking fault $a/6 [1\bar{2}10] + \alpha c [0001]$ with $\alpha \neq 0$, a minimum also predicted by a simple hard sphere model.⁴² This minimum either disappears or is located exactly in $a/6 [1\bar{2}10]$ ($\alpha = 0$) only when the angular dependence of the atomic interactions is taken into account. The value γ_p of the stacking fault energy obtained with Mendelev and Ackland EAM potential²⁴ for this minimum is much lower than our *ab initio* value (Tab. II). This is quite normal as Mendelev and Ackland used the *ab initio* value of Domain *et al.* to fit their potential.

C. Dislocation dissociation

Before using atomistic simulations to obtain dislocation core structures and their associated Peierls stress, it is worth looking what can be learned from these γ -surface calculations. Legrand⁵ proposed a criterion based on the elastic constants and the metastable stacking fault energies to determine if glide occurs in the base or prism plane in a hcp crystal. According to this criterion, prismatic glide is favored if the ratio $R = C_{66}\gamma_b/C_{44}\gamma_p$ is larger than 1. Tab II shows that this is the case for the EAM potential and the PWSCF calculation, as well as for the VASP calculation of Domain *et al.*²⁸ and of Udagawa

*et al.*³⁷ On the other hand, SIESTA leads to a value too close to 1 to be able to decide between basal and prismatic glide.

One can also use dislocation elasticity theory⁴³ to compute the dissociation distance of a dislocation both in the basal and prism planes. According to elasticity theory, the energy variation caused by a dissociation of length d is

$$\Delta E_{\text{diss}}(d) = -b_i^{(1)} K_{ij} b_j^{(2)} \ln \left(\frac{d}{r_c} \right) + \gamma d, \quad (3)$$

where $\mathbf{b}^{(1)}$ and $\mathbf{b}^{(2)}$ are the Burgers vectors of each partial dislocation, γ the corresponding stacking fault energy, K the Stroh matrix^{44,45} controlling dislocation elastic energy, and r_c the core radius. Minimization of this energy leads to the equilibrium dissociation length

$$d^{\text{eq}} = \frac{b_i^{(1)} K_{ij} b_j^{(2)}}{\gamma}. \quad (4)$$

When the hcp crystal is oriented with the x , y , and z axis respectively along the $[10\bar{1}0]$, $[0001]$, and $[1\bar{2}10]$ directions, for a dislocation lying along the z direction, the K matrix is diagonal with its components given by^{46-48,49}

$$\begin{aligned} K_{11} &= \frac{1}{2\pi} (\bar{C}_{11} + C_{13}) \sqrt{\frac{C_{44} (\bar{C}_{11} - C_{13})}{C_{33} (\bar{C}_{11} + C_{13} + 2C_{44})}}, \\ K_{22} &= \sqrt{\frac{C_{33}}{C_{11}}} K_{11}, \\ K_{33} &= \frac{1}{2\pi} \sqrt{\frac{1}{2} C_{44} (C_{11} - C_{12})}, \end{aligned}$$

where $\bar{C}_{11} = \sqrt{C_{11} C_{33}}$.

The γ -surface of the basal plane (Fig. 1) indicates a possible dissociation $1/3[1\bar{2}10] \rightarrow 1/3[1\bar{1}00] + 1/3[0\bar{1}10]$. The dissociation length in the basal plane is then, for a $1/3[1\bar{2}10]$ screw dislocation,

$$d_b^{\text{eq}} = \frac{(3K_{33} - K_{11}) a^2}{12\gamma_b}. \quad (5)$$

According to the minimum of the γ -surface in the prism plane (Fig. 3), a $1/3[1\bar{2}10]$ dislocation can dissociate in this plane in two partial dislocations with Burgers vectors $1/6[1\bar{2}10] \pm \alpha c/a[0001]$. The parameter α controls the position of the stacking fault minimum along the $[0001]$ direction, *i.e.* $\alpha = 0$ for PWSCF and SIESTA, and $\alpha = 0.14$ for the EAM potential. The dissociation length of a screw dislocation in the prism plane is then

$$d_p^{\text{eq}} = \frac{(K_{33}a^2 - 4\alpha^2 K_{22}c^2)}{4\gamma_p}. \quad (6)$$

The dissociation lengths d_b^{eq} and d_p^{eq} calculated from the elastic constants and the stacking fault energies are given in table II. Elastic constants predicted by the atomic interaction models are used in each case. For all

energy models, one expects a larger dissociation in the prism than in the basal plane. We will compare in the following section these dissociation lengths predicted by elasticity theory with the ones observed in our atomistic simulations of the dislocation core structure.

IV. SCREW DISLOCATION CORE

A. Methodology

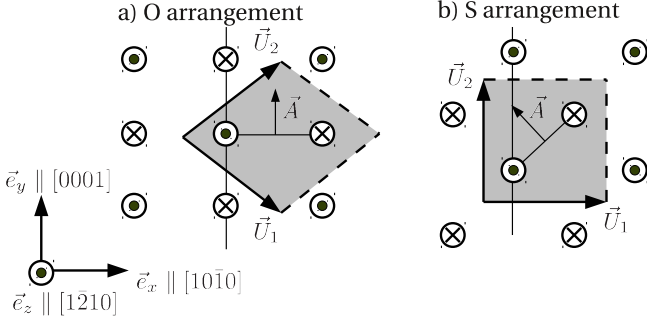


FIG. 5. Screw dislocation periodic arrangements used for atomistic simulations. \vec{U}_1 and \vec{U}_2 are the periodicity vectors of the arrangement, and \vec{A} the cut vector of the dislocation dipole. The thin vertical line corresponds to the prism glide plane.

Our atomistic simulations of the core structure of a screw dislocation are based on full periodic boundary conditions.⁵⁰ This requires introducing a dislocation dipole in the simulation cell. Two periodic arrangements of the dislocations have been used (Fig. 5). In the O arrangement, dislocations with opposite Burgers vectors are located on the same prism and basal planes, *i.e.* the two foreseen glide planes. On the other hand, only dislocation with the same Burgers vectors can be found on a given prism or basal plane in the S arrangement.

Periodicity vectors of the O arrangement are, before introducing the dislocations, $\vec{U}_1 = na\frac{1}{2}[10\bar{1}0] - mc[0001]$, $\vec{U}_2 = na\frac{1}{2}[10\bar{1}0] + mc[0001]$, and $\vec{U}_3 = a\frac{1}{3}[1\bar{2}10]$. The integers n and m are taken equal to keep an aspect ratio close to a square. This simulation cell has been used for *ab initio* calculations with $n = 4$ (128 atoms), $n = 5$ (160 atoms), and $n = 6$ (288 atoms).

For the S arrangement, $\vec{U}_1 = na\frac{1}{2}[10\bar{1}0]$, $\vec{U}_2 = mc[0001]$, and $\vec{U}_3 = a\frac{1}{3}[1\bar{2}10]$. *Ab initio* calculations have been performed with $n = m$ and varying between $n = 5$ (100 atoms) and $n = 8$ (256 atoms).

Both dislocation arrays are quadrupolar: the vector joining the two dislocations composing the primitive dipole is $\vec{D} = 1/2(\vec{U}_1 + \vec{U}_2)$. Because of the centrosymmetry of this arrangement and the symmetry properties of the Volterra elastic field, this ensures that the stress created by other dislocations is minimal at each dislocation position. The cut vector \vec{A} defining the dislocation

dipole is obtained by a $\pi/2$ rotation of \vec{D} .

The dislocation dipole is introduced in the simulation cells by applying to all atoms the elastic displacement predicted by anisotropic elasticity theory^{44,45} taking full account of the periodic boundary conditions.⁵¹ A homogeneous strain is also applied to the simulation cell so as to cancel the plastic strain introduced by the dislocation dipole and minimize the elastic energy. This strain is given by

$$\varepsilon_{ij}^0 = -\frac{b_i A_j + b_j A_i}{2S},$$

where $S = |(\vec{U}_1 \wedge \vec{U}_2) \cdot \vec{e}_z|$ is the surface of the simulation cell perpendicular to the dislocation lines. This homogeneous strain adds some tilt components to the periodicity vectors. Atoms are then relaxed until all components of the atomic forces are smaller than $5 \text{ meV } \text{\AA}^{-1}$ for SIESTA, $2 \text{ meV } \text{\AA}^{-1}$ for PWSCF, and $0.1 \text{ meV } \text{\AA}^{-1}$ for the EAM potential.

B. Core structure

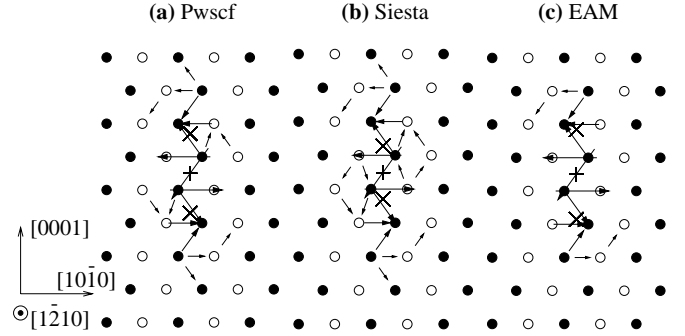


FIG. 6. Differential displacement maps around one of the two $1/3[1\bar{2}10]$ screw dislocations composing the dipole for the S periodic arrangement with $n = m = 7$ (196 atoms). Atoms are sketched by circles with a color depending on the $(1\bar{2}10)$ plane to which they belong. The arrow between two atomic columns is proportional to the $[1\bar{2}10]$ component of the differential displacement between the two atoms. Displacements smaller than $0.1b$ are not shown. Crosses \times correspond to the positions of the two partial dislocations, and $+$ to their middle, *i.e.* the position of the total dislocation.

Starting from perfect dislocations, atom relaxation leads to dislocations spread in the prism plane, whatever the interaction model (EAM, SIESTA, or PWSCF) and whatever the simulation cell used. This can be clearly seen by plotting differential displacement maps as introduced by Vitek.⁵² These maps (Fig. 6) show that the strain created by the screw dislocation spreads out in the $(10\bar{1}0)$ prism plane and that displacements outside this plane are much smaller.

To characterize this spreading in the $(10\bar{1}0)$ prism plane, we extract from our atomistic simulations the disregistry $D(x)$ created by the dislocation. This is de-

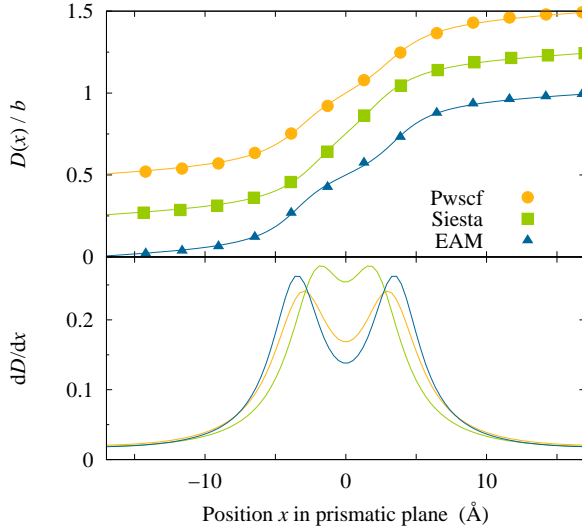


FIG. 7. Disregistry $D(x)$ created by the screw dislocation in the prism plane and corresponding dislocation density $\rho(x) = \partial D(x)/\partial x$ for the S periodic arrangement with 196 atoms ($n = m = 7$). Symbols correspond to atomistic simulations and lines to the fit of the Peierls-Nabarro model to these data. For clarity, disregistries $D(x)$ have been shifted by 0.25 between the different interaction models.

defined as the displacement difference between the atoms in the plane just above and those just below the dislocation glide plane. The derivative of this function, $\rho(x) = \partial D/\partial x$ corresponds to the dislocation density. Fig. 7 shows the disregistry obtained for the three interaction models. In all cases, the b discontinuity created by the screw dislocation does not show a sharp interface, but spreads on a distance ~ 10 Å.

Peierls⁵³ and Nabarro⁵⁴ built a model that leads to a simple expression of the disregistry. The analytical expression they obtained⁴³ can be extended to a dissociated dislocation. As suggested by the prismatic γ -surface (Fig. 3), we assume that the screw dislocation dissociates in two equivalent partial dislocation separated by a distance d . Based on the Peierls-Nabarro model, we write the disregistry created by a single dislocation

$$D_{\text{dislo}}(x) = \frac{b}{2\pi} \left\{ \arctan \left[\frac{x - x_0 - d/2}{\zeta} \right] + \arctan \left[\frac{x - x_0 + d/2}{\zeta} \right] + \pi/2 \right\}, \quad (7)$$

where x_0 is the dislocation position, d its dissociation length, and ζ the spreading of each partial dislocation. We need then to take into account that we do not have only one dislocation on a given prism plane but a periodic array (Fig. 5). The disregistry created by an array of

period L is

$$D_L(x) = \sum_{n=-\infty}^{\infty} D_{\text{dislo}}(x - nL) \\ = \frac{b}{2\pi} \left\{ \arctan \left[\frac{\tan \left(\frac{\pi}{L} [x - x_0 - d/2] \right)}{\tanh \left(\frac{\pi \zeta}{L} \right)} \right] + \pi \left\lfloor \frac{x - x_0 - d/2}{L} + \frac{1}{2} \right\rfloor + \arctan \left[\frac{\tan \left(\frac{\pi}{L} [x - x_0 + d/2] \right)}{\tanh \left(\frac{\pi \zeta}{L} \right)} \right] + \pi \left\lfloor \frac{x - x_0 + d/2}{L} + \frac{1}{2} \right\rfloor \right\}, \quad (8)$$

where $\lfloor \cdot \rfloor$ is the floor function. For the O arrangement (Fig. 5a), the disregistry in the prism plane should be given by $D(x) = D_L(x) - D_L(x - L/2)$ with $L = 2mc$, whereas it should be $D(x) = D_L(x)$ with $L = mc$ for the S arrangement (Fig. 5b).

We fit this analytical expression of the dislocation disregistry to the data coming from the atomistic simulations. Fig. 7 shows a good agreement between atomistic simulations and the model, using only three fitting parameters: the dislocation position x_0 , the dissociation length d and the spreading ζ . This procedure therefore allows us to determine the location of the dislocation center. For all interaction models, we find that this center lies in between two (0001) atomic planes. One can see in Fig. 6 that this position corresponds to a local symmetry axis of the differential displacement map. This is different from the result obtained by Ghazisaeidi and Trinkler¹³ in Ti where the center of the screw dislocation was found to lie exactly in one (0001) atomic plane, a position that corresponds in Zr to the saddle point between two Peierls valleys, as it will be shown below.

The dissociation length of the screw dislocation obtained through this fitting procedures are shown in Fig. 8 for both periodic arrangements. We observe variations with the dislocation periodic arrangement used in the simulation, as well as with the size of the simulation cell. The results are nevertheless close to the predictions of elasticity theory (§III C) for all the three interaction models. We could even see with the EAM potential that the dissociation lengths extracted from atomistic simulations converge to the value given by elasticity theory for large enough unit cells. It is thus relevant to describe the screw dislocation as dissociated in two partial dislocations linked by a stacking fault, although the dissociation length remains small.

C. Core energy

We obtain the dislocation core energy by subtracting the elastic energy from the excess energy given by the

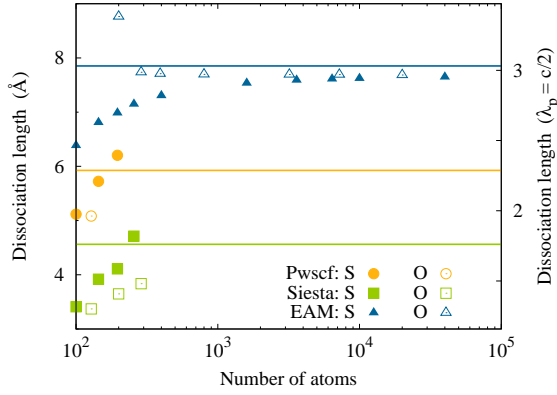


FIG. 8. Dissociation length of the screw dislocation. Symbols correspond to data extracted from atomistic simulations through the fit of the disregistry (Eq. 8) for both the O and S periodic arrangements and for different sizes of the simulation cell. The solid lines are the predictions of elasticity theory based on the stacking faults (Tab. II). On the right vertical axis, the experimental c lattice parameter has been used to normalized the dissociation length by the distance $\lambda_p = c/2$ between Peierls valleys.

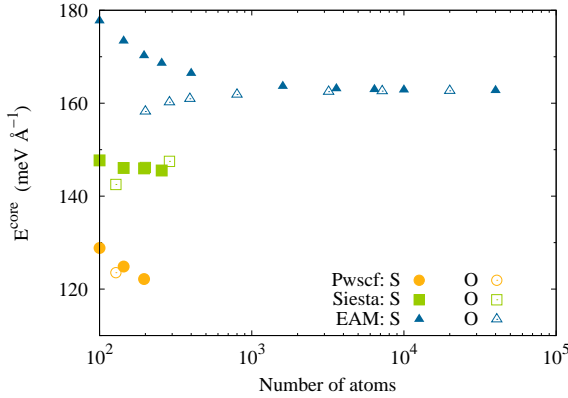


FIG. 9. Core energy of the screw dislocation obtained for different sizes of the atomistic simulation cell and for both the O and S periodic arrangements ($r_c = b$).

atomistic simulations. This excess energy is the energy difference between the simulation cell containing the dislocation dipole and the same cell without any defect. The elastic energy calculation takes into account the elastic anisotropy^{44,45} and the effect of periodic boundary conditions.⁵¹ The obtained core energy are shown in Fig. 9. Like for the dissociation length, some variations with the size of the simulation cell and the periodic arrangement can be observed. We did not manage to link both quantities, *i.e.* the core energy and the dissociation length. They are not simply related by the expression of the energy variation with the dissociation length (Eq. 3), and the change of the elastic interaction between dislocations caused by their dissociation could not fully explain the variation of the core energy either. As the spread-

ing of partial dislocations also depends on the size of the simulation cells, the variation of the core energy probably have a more complex origin than simply a variation of the dissociation length.

We could use, with the EAM potential, a simulation cell large enough to obtain a converged value of the core energy, $163 \text{ meV } \text{\AA}^{-1}$ for a core radius $r_c = b$. It is worth pointing that this value does not depend on the periodic arrangement used in the simulation (Fig. 9). This can be achieved thanks to a proper account of the core traction contribution to the elastic energy.⁵⁵ A difference of $\sim 10 \text{ meV } \text{\AA}^{-1}$ would have been observed between the S and O periodic arrangement without this contribution. *Ab initio* calculations lead to a dislocation core energy of $145 \pm 5 \text{ meV } \text{\AA}^{-1}$ for SIESTA and $125 \pm 5 \text{ meV } \text{\AA}^{-1}$ for PWSCF ($r_c = b$ in both cases).

D. Dissociation in the basal plane

Basal slip is observed experimentally only at high temperature (above 850 K) and for a higher resolved shear stress than the one needed to activate prismatic slip.⁵⁶ At lower temperatures, no basal slip could be observed,^{3,57} even when the monocrystal was oriented so as to favor basal slip. Our atomistic simulations lead to a screw dislocation configuration dissociated in the prism plane, which clearly cannot glide easily in the basal plane. It is worth looking if another configuration, which could glide in this basal plane, also exists.

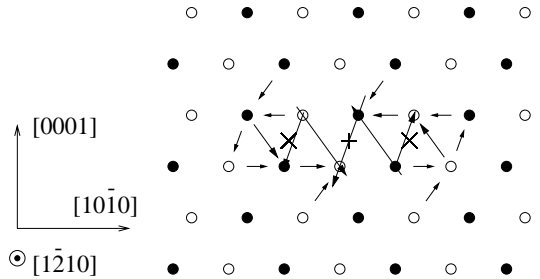


FIG. 10. Differential displacement map of the metastable configuration of a $1/3[1210]$ screw dislocation dissociated in the basal plane, as obtained with the EAM potential for the O periodic arrangement with $n = 6$ (288 atoms). Crosses \times correspond to the positions of the two partial dislocations, and $+$ to their middle, *i.e.* the position of the total dislocation.

Using the same EAM potential, Khater and Bacon²⁵ showed that a screw dislocation can also dissociate in the basal plane. The basal configuration is obtained by introducing in the same basal plane two partial dislocations of Burgers vector $1/3[1\bar{1}00]$ and $1/3[0\bar{1}10]$, in agreement with the location of the minimum on the basal γ -surface (Fig. 1). After relaxation of the atomic positions, the dislocation remains dissociated in the basal plane, as can be seen from the corresponding differential displacement map (Fig. 10). A fit of the screw component of the disregistry created by the dislocation in the basal plane

leads to a dissociation length $d = 6.0 \text{ \AA}$, a higher value than predicted by elasticity theory (Tab. II). This configuration is metastable. It has indeed an energy higher by 62 meV \AA^{-1} than the configuration dissociated in the prism plane.

We check if *ab initio* calculations also lead to such a metastable configuration. Starting from a screw dislocation dissociated in two partial dislocations in the basal plane, both SIESTA and PWSCF lead after relaxation of the atomic positions to the stable configuration dissociated in the prism plane. This is true both with the S ($n = 5$) and the O ($n = 4$) periodic arrangements. These *ab initio* calculations show then that such a dissociation of the screw dislocation in the basal plane is unstable. The metastable configuration observed with the EAM potential appears to be an artifact of the empirical potential. This is not specific to the Mendeleev and Ackland potential²⁴ as a configuration dissociated in the basal plane is stabilized by any central forces potential.^{25,41,58}

V. PEIERLS BARRIER

Before calculating *ab initio* the Peierls barrier of the screw dislocation, we use the EAM potential to assess the validity of the method and to check the convergence of the Peierls barrier with the size of the simulation cell.

A. Methodology

We determine the Peierls barrier for the screw dislocation gliding in the prism plane. This is done using a constrained minimization between two adjacent equilibrium configurations of the dislocations. We move both dislocations in the same direction by one Peierls distance $\lambda_P = c/2$ between the initial and final states, so as to keep constant the distance between dislocations.

Two different algorithms are used to perform the constrained minimization, the simple drag method and the more robust nudged elastic band (NEB) method.⁵⁹ Intermediate configurations are built by linearly interpolating the atomic coordinates between the initial and final states. We define the corresponding reaction coordinate $\zeta = (\vec{X} - \vec{X}^I) \cdot (\vec{X}^F - \vec{X}^I) / \|\vec{X}^F - \vec{X}^I\|^2$, where \vec{X} , \vec{X}^I , and \vec{X}^F are the $3N$ vectors defining atomic positions for respectively the intermediate, initial, and final configurations. In the drag method, the minimization is performed on all atomic coordinates with the constraint that ζ remains fixed for each of the nine intermediate images. Nine intermediate images are also used in NEB method with a spring constant $k = 0.1 \text{ eV \AA}^{-2}$.

So as to obtain the variation along the path of the dislocation energy with its position, we need to determine the dislocation position $x_{\text{Dislo}}(\zeta)$ for each intermediate image, once it has been relaxed. This is done thanks to a fit of the disregistry in the prism plane, as described in §IV B. This allows us to check that both dislocations

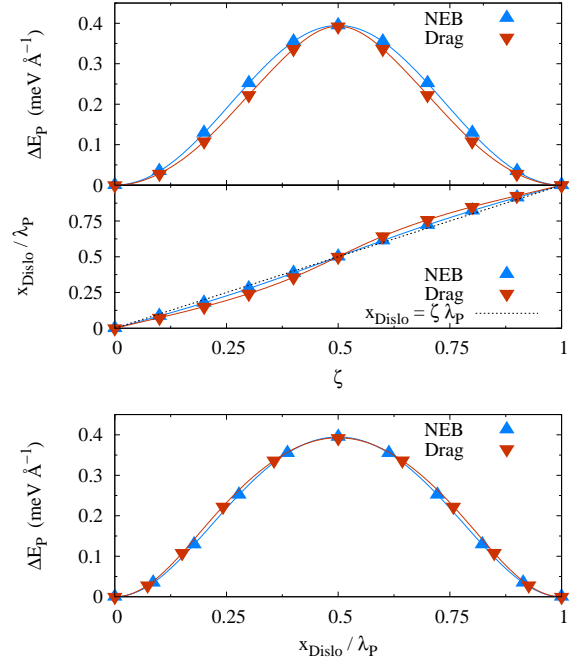


FIG. 11. Peierls barrier of a screw dislocation calculated with the EAM potential for the S periodic arrangement with 1600 atoms ($n = m = 20$). Two different methods for finding the minimum energy path have been used: the NEB method and a simple constrained minimization (drag). Symbols correspond to the results of atomistic simulations and lines to their interpolation with Fourier series.

in the simulation cell are moving in a coordinated way: the distance between them remains fixed. As a consequence, there is no variation of the elastic energy along the path and the energy variation $\Delta E_P(\zeta)$ obtained by the constrained minimization corresponds to a variation of the core energy, *i.e.* the Peierls energy. We deduce the Peierls energy $\Delta E_P(x_{\text{Dislo}})$ by eliminating the reaction coordinate ζ between $\Delta E_P(\zeta)$ and $x_{\text{Dislo}}(\zeta)$.

Fig. 11 illustrates the whole procedure for a given dislocation periodic arrangement using both constrained minimization techniques. The variation $\Delta E_P(\zeta)$ slightly differs between both techniques: for a given reaction coordinate ζ , the drag method leads to a state of lower energy than NEB method. This corresponds to a small difference in the dislocation position: this position deviates more with drag than with NEB method from a linear variation. Nevertheless, one obtains at the end the same Peierls barrier $\Delta E_P(x_{\text{Dislo}})$, whatever the method used. These differences observed for the functions $\Delta E_P(\zeta)$ and $x_{\text{Dislo}}(\zeta)$ between drag and NEB methods increase with the size of the simulation cell, *i.e.* with the number of degrees of liberty. For large simulation cells (containing more than 3600 atoms in the S periodic arrangement for instance), the drag method sometimes fails to find a continuous path between the initial and final states: one has to use the NEB method in these cases. Only much

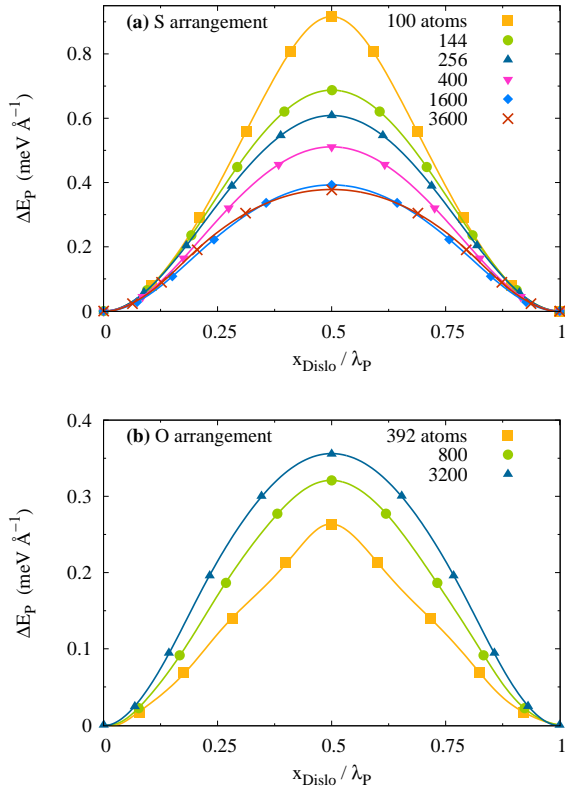


FIG. 12. Variation of the Peierls barrier with the size of the simulation cell calculated with the EAM potential for both periodic arrangements.

smaller simulation cells can be studied *ab initio*. For these sizes, the drag and the NEB methods always lead to the same result. We will therefore only use the drag method in the *ab initio* calculations, as it costs much less CPU time.

Finally, we interpolate with Fourier series the periodic functions $\Delta E_P(\zeta)$ and $x_{\text{Dislo}}(\zeta) - \lambda_P \zeta$. This leads to a smooth function $\Delta E_P(x_{\text{Dislo}})$ that can be derived. The Peierls stress σ_P is deduced from the maximal slope of this function,

$$\sigma_P = \frac{1}{b} \text{Max} \left(\frac{\partial \Delta E_P}{\partial x_{\text{Dislo}}} \right). \quad (9)$$

We obtain a Peierls stress $\sigma_P = 24 \pm 1 \text{ MPa}$ for the EAM potential. Khater and Bacon²⁵ determined, for the same empirical potential, a Peierls stress $\sigma_P = 22 \text{ MPa}$ using molecular statics simulations under applied stress. As the agreement between both methods is good, we see that the Peierls stress can be defined either from the slope of the Peierls barrier or from the minimal applied stress under which the dislocation glides indefinitely.

We now examine, still with the EAM potential, how this Peierls barrier varies when the size of the simulation cell decreases up to reaching a number of atoms that can be handled in *ab initio* calculations (Fig. 12). Both the S

and O periodic arrangements give the same Peierls barrier, and hence the same Peierls stress, for a large enough simulation cell ($\gtrsim 1000$ atoms). The Peierls barrier increases when the size of the simulation cell decreases with the S periodic arrangement, whereas it decreases with the O periodic arrangement. As a consequence, the S and O periodic arrangement should respectively lead to an upper and lower limits of the Peierls stress for small simulation cells. We will therefore use the S periodic arrangement to calculate *ab initio* this Peierls barrier. This will allow us to confirm that the Peierls stress is as low as indicated by experiments and this EAM potential. Moreover, it is worth pointing that the expected Peierls barrier should be small: $\Delta E_P = 0.4 \text{ meV } \text{\AA}^{-1}$ at the saddle point according to the EAM potential. This corresponds to a difference of energy $2b\Delta E_P = 2.6 \text{ meV}$ for a simulation cell of minimal height containing a dislocation dipole. Such a small energy difference may be problematic because of the precision of *ab initio* calculations. Looking for an upper limit of this value is easier as it minimizes the problems associated with this precision.

Finally, it is worth pointing that the dissociation length varies during the dislocation migration, and this variation is more pronounced ($\sim 10\%$) for the smallest simulation cells. But, like for the core energy, we did not manage to relate the size dependence of the Peierls barrier to this variation of the dissociation length.

B. *Ab initio* barriers

The Peierls barriers obtained by *ab initio* calculations are shown on Fig. 13(a) for PWSCF and Fig. 13(b) for SIESTA. In both cases, the height of the barrier decreases when the number of atoms increases, in agreement with what has been observed with the EAM potential for the same S periodic arrangement. For a given number of atoms, the *ab initio* barriers are a little bit lower than the ones obtained with the EAM potential. Results obtained with SIESTA are noisy: the energy barrier that we want to calculate is so small that it needs a really strict convergence criterion on atomic forces for the relaxation. We did not manage to reach such a precision with SIESTA. On the other hand, the barriers obtained with PWSCF are smooth. We can therefore interpolate the *ab initio* results with Fourier series, and estimate then the Peierls stress (Eq. 9). This leads to $\sigma_P = 36 \text{ MPa}$ for the simulation cell containing 100 atoms and $\sigma_P = 21 \text{ MPa}$ for 144 atoms. Considering that these values, obtained in small simulation cells, are upper limits, *ab initio* calculations predict a Peierls stress smaller than 21 MPa for a screw dislocation in zirconium gliding in a prism plane.

The comparison of this *ab initio* estimate of the Peierls stress with experimental data^{2,3,19,57} is quite challenging. As pointed out in the introduction, the yield stress of zirconium strongly depends on its oxygen content. No experimental data exists for a purity better than 0.07% O (in atomic fraction). Moreover, all measure-

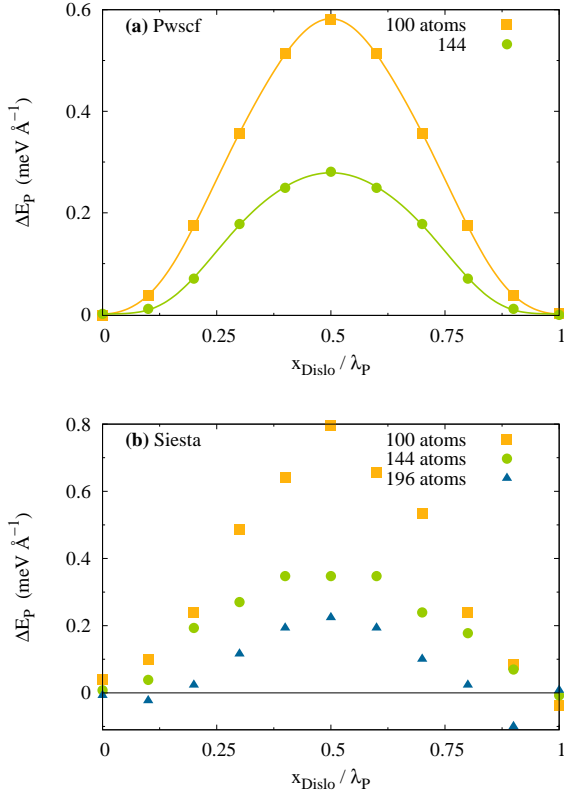


FIG. 13. Peierls barrier for a screw dislocation gliding in its prism plane calculated *ab initio* with (a) PWSCF and (b) SIESTA for the S periodic arrangement. Symbols correspond to *ab initio* results and lines to their interpolation by Fourier series.

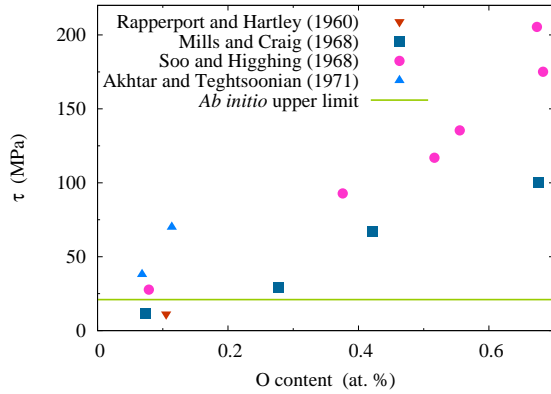


FIG. 14. Zirconium flow stress determined experimentally for various O contents.^{2,3,19,57} Data have been extrapolated to 0 K and are compared to the *ab initio* Peierls stress of screw dislocations in pure Zr.

ments have been performed at temperatures higher than 77 K. The determination of pure zirconium flow stress at 0 K therefore needs some extrapolation of experimental data. Without a clear understanding of the mechanisms responsible of zirconium hardening by oxygen impurities, such an extrapolation is quite hazardous. Nevertheless, a graphical comparison (Fig. 14) of experimental data with our *ab initio* Peierls stress shows a reasonable agreement, keeping in mind that the value 21 MPa has to be considered as an upper limit.

VI. CONCLUSIONS

Using two *ab initio* approaches (PWSCF and SIESTA), both in the DFT-GGA approximation, we have shown that a $1/3\langle 1\bar{2}10 \rangle$ screw dislocation in hcp zirconium dissociates in two partial dislocations with a pure screw character. This is in agreement with the minimum in $1/6\langle 1\bar{2}10 \rangle$ found for the generalized stacking fault energy in the prism plane. We could extract the dissociation length from our atomistic simulations. Although this dissociation length is small ($d \sim 6 \text{ \AA}$ for PWSCF and $d \sim 4 \text{ \AA}$ for SIESTA), it is in reasonable agreement with the one predicted by elasticity theory.

The EAM potential of Mendelev and Ackland²⁴ leads to the same structure of the dislocation dissociated in the prism plane. The metastable configuration dissociated in the basal plane predicted by this potential is not stable in *ab initio* calculations, both with PWSCF and SIESTA. This configuration is therefore an artifact of this potential, probably induced by the deep minimum in $1/3\langle 1\bar{1}00 \rangle$ found with this empirical potential for the generalized stacking fault in the basal plane. This minimum is much more shallow in *ab initio* calculations.

We could also obtain an *ab initio* estimate of the Peierls stress of the screw dislocation gliding in the prism plane. Calculations with PWSCF lead to an upper limit of 21 MPa for this Peierls stress. This small value shows that screw dislocations can glide quite easily in pure zirconium, thus confirming what had been obtained with Mendelev and Ackland EAM potential. Such a small Peierls stress is in agreement with experimental data, once the hardening of oxygen impurities has been considered.

ACKNOWLEDGMENTS

This work was performed using HPC resources from GENCI-CINES and GENCI-CCRT (Grant Nos 2011-096020 and 2012-096847).

* emmanuel.clouet@cea.fr

¹ E. Rappoport, Acta Metall. **7**, 254 (1959).

² P. Soo and G. T. Higgins, Acta Metall. **16**, 177 (1968).

³ A. Akhtar and A. Teghtsoonian,

- Acta Metall. **19**, 655 (1971).
- ⁴ D. Caillard and J. L. Martin, *Thermally Activated Mechanisms in Crystal Plasticity*, edited by R. W. Cahn (Pergamon, Amsterdam, 2003).
 - ⁵ B. Legrand, Philos. Mag. B **49**, 171 (1984).
 - ⁶ B. Legrand, Philos. Mag. A **54**, 43 (1986).
 - ⁷ B. Legrand, Philos. Mag. A **52**, 83 (1985).
 - ⁸ A. Girshick, D. G. Pettifor, and V. Vitek, Philos. Mag. A **77**, 999 (1998).
 - ⁹ F. Ferrer, A. Barbu, T. Bretheau, J. Crepin, F. Willaime, and D. Charquet, in *Zirconium in the nuclear industry: thirteenth international symposium*, American Society for Testing and Materials Special Technical Publication, Vol. 1423, edited by G. D. Moan and P. Rudling (American Society Testing and Materials, W Conshohocken, USA, 2002) pp. 863–885, 13th International Symposium on Zirconium in the Nuclear Industry, Annecy, France, June 10–14, 2001.
 - ¹⁰ C. Domain and A. Legris, in *Mat. Res. Soc. Symp. Proc.*, Vol. 653 (2001) p. Z3.8.
 - ¹¹ C. Domain, J. Nucl. Mater. **351**, 1 (2006).
 - ¹² N. Tarrat, M. Benoit, and J. Morillo, Int. J. Mater. Res. **100**, 329 (2009).
 - ¹³ M. Ghazisaeidi and D. Trinkle, Acta Mater. **60**, 1287 (2012).
 - ¹⁴ V. Vitek and V. Paidar, in *Dislocations in Solids*, Vol. 14, edited by J. Hirth (Elsevier, 2008) Chap. 87, pp. 439–514.
 - ¹⁵ J. Bailey, J. Nucl. Mater. **7**, 300 (1962).
 - ¹⁶ S. Naka, A. Lasalmonie, P. Costa, and L. P. Kubin, Philos. Mag. A **57**, 717 (1988).
 - ¹⁷ S. Farenc, D. Caillard, and A. Couret, Acta Metall. Mater. **41**, 2701 (1993).
 - ¹⁸ S. Farenc, D. Caillard, and A. Couret, Acta Metall. Mater. **43**, 3669 (1995).
 - ¹⁹ D. Mills and G. B. Craig, Trans. AIME **242**, 1881 (1968).
 - ²⁰ D. H. Sastry, Y. V. R. K. Prasad, and K. I. Vasu, J. Mater. Sci. **6**, 332 (1971).
 - ²¹ D. Sastry and K. Vasu, Acta Metall. **20**, 399 (1972).
 - ²² T. Tanaka and H. Conrad, Acta Metall. **20**, 1019 (1972).
 - ²³ A. Akhtar and E. Teghtsoonian, Metall. Mater. Trans. A **6**, 2201 (1975).
 - ²⁴ M. I. Mendelev and G. J. Ackland, Philos. Mag. Lett. **87**, 349 (2007).
 - ²⁵ H. A. Khater and D. J. Bacon, Acta Mater. **58**, 2978 (2010).
 - ²⁶ J. M. Soler, E. Artacho, J. D. Gale, A. García, J. Junquera, P. Ordejón, and D. Sánchez-Portal, J. Phys.: Condens. Matter **14**, 2745 (2002).
 - ²⁷ P. Giannozzi, S. Baroni, N. Bonini, M. Calandra, R. Car, C. Cavazzoni, D. Ceresoli, G. L. Chiarotti, M. Cococcioni, I. Dabo, A. Dal Corso, S. de Gironcoli, S. Fabris, G. Fratesi, R. Gebauer, U. Gerstmann, C. Gougousis, A. Kokalj, M. Lazzeri, L. Martin-Samos, N. Marzari, F. Mauri, R. Mazzarello, S. Paolini, A. Pasquarello, L. Paulatto, C. Sbraccia, S. Scandolo, G. Sclauzero, A. P. Seitsonen, A. Smogunov, P. Umari, and R. M. Wentzcovitch, J. Phys.: Condens. Matter **21**, 395502 (2009).
 - ²⁸ C. Domain, R. Besson, and A. Legris, Acta Mater. **52**, 1495 (2004).
 - ²⁹ G. Vértité, F. Willaime, and C. C. Fu, Solid State Phenom. **129**, 75 (2007).
 - ³⁰ Pseudopotential file Zr.pbe-nsp-van.UPF from www.quantum-espresso.org.
 - ³¹ C. S. G. Cousins, J. Phys. C Solid State **12**, 989 (1979).
 - ³² P. Villars and L. D. Calvert, *Pearson's Handbook of Crystallographic Data for Intermetallic Phases* (American Society for Metals, OH, 1985).
 - ³³ C. Stassis, J. Zarestky, D. Arch, O. D. McMasters, and B. N. Harmon, Phys. Rev. B **18**, 2632 (1978).
 - ³⁴ E. S. Fisher and C. J. Renken, Phys. Rev. **135**, A482 (1964).
 - ³⁵ Elastic constants calculated by Mendelev and Ackland in the original article describing the EAM potential²⁴ did not take into account atomic relaxations. This explains the difference with the ones given in Tab. I.
 - ³⁶ V. Vitek, Philos. Mag. **18**, 773 (1968).
 - ³⁷ Y. Udagawa, M. Yamaguchi, H. Abe, N. Sekimura, and T. Fuketa, Acta Mater. **58**, 3927 (2010).
 - ³⁸ D. Hull and D. J. Bacon, *Introduction to Dislocations*, 4th ed. (Butterworth Heinemann, 2001).
 - ³⁹ See Supplemental Material at <http://link.aps.org/supplemental/10.1103/PhysRevB.86.144104> for a discussion on the convergence of this fault energy with PWSCF parameters.
 - ⁴⁰ G. J. Ackland, S. J. Wooding, and D. J. Bacon, Philos. Mag. A **71**, 553 (1995).
 - ⁴¹ D. Bacon and V. Vitek, Metall. Mater. Trans. A **33**, 721 (2002).
 - ⁴² K. Schwartzkopff, Acta Metall. **17**, 345 (1969).
 - ⁴³ J. P. Hirth and J. Lothe, *Theory of Dislocations*, 2nd ed. (Wiley, New York, 1982).
 - ⁴⁴ A. N. Stroh, Philos. Mag. **3**, 625 (1958).
 - ⁴⁵ A. N. Stroh, J. Math. Phys. (Cambridge, Mass.) **41**, 77 (1962).
 - ⁴⁶ A. J. E. Foreman, Acta Metall. **3**, 322 (1955).
 - ⁴⁷ L. J. Teutonico, Mater. Sci. Eng. **6**, 27 (1970).
 - ⁴⁸ M. M. Savin, V. M. Chernov, and A. M. Strokova, Phys. Status Solidi A **35**, 747 (1976).
 - ⁴⁹ Foreman⁴⁶ gave a different expression for K_{22} , but the comparison with a numerical evaluation of the K matrix using Stroh formalism^{44,45} shows that the correct expression is the one given by Savin *et al.*⁴⁸.
 - ⁵⁰ V. V. Bulatov and W. Cai, *Computer Simulations of Dislocations*, edited by A. P. Sutton and R. E. Rudd, Oxford series on materials modelling (Oxford University Press, 2006).
 - ⁵¹ W. Cai, V. V. Bulatov, J. Chang, J. Li, and S. Yip, Philos. Mag. **83**, 539 (2003).
 - ⁵² V. Vitek, R. C. Perrin, and D. K. Bowen, Philos. Mag. **21**, 1049 (1970).
 - ⁵³ R. Peierls, Proc. Phys. Soc. **52**, 34 (1940).
 - ⁵⁴ F. R. N. Nabarro, Proc. Phys. Soc. **59**, 256 (1947).
 - ⁵⁵ E. Clouet, Philos. Mag. **89**, 1565 (2009).
 - ⁵⁶ A. Akhtar, Acta Metall. **21**, 1 (1973).
 - ⁵⁷ K. E. J. Rapperport and C. S. Hartley, Trans. AIME **218**, 869 (1960).
 - ⁵⁸ M. H. Liang and D. J. Bacon, Philos. Mag. A **53**, 181 (1986).
 - ⁵⁹ G. Henkelman, G. Jóhannesson, and H. Jónsson, in *Progress in Theoretical Chemistry and Physics*, Vol. 5, edited by S. D. Schwartz (Springer Netherlands, 2000) Chap. 10, pp. 269–302.